Astronomy & Astrophysics manuscript no. paper
September 8, 2020

The elusive tidal tails of the Milky Way globular cluster NGC 7099

Andrés E. Piatti[1,2⋆], Julio A. Carballo-Bello[3], Marcelo D. Mora[4], Carolina Cenzano[4], Camila Navarrete[5,6], and Márcio Catelan[4,6]

[1] Instituto Interdisciplinario de Ciencias Básicas (ICB), CONICET-UNCUYO, Padre J. Contreras 1300, M5502JMA, Mendoza, Argentina
[2] Consejo Nacional de Investigaciones Científicas y Técnicas (CONICET), Godoy Cruz 2290, C1425FQB, Buenos Aires, Argentina
[3] Instituto de Alta Investigación, Universidad de Tarapacá, Casilla 7D, Arica, Chile
[4] Instituto de Astrofísica, Facultad de Física, Pontificia Universidad Católica de Chile, Av. Vicuña Mackenna 4860, 782-0436 Macul, Santiago, Chile
[5] European Southern Observatory, Alonso de Córdova 3107, Casilla 19001, Santiago, Chile
[6] Millenium Institute of Astrophysics, Santiago, Chile

Received / Accepted

ABSTRACT

We present results on the extra-tidal features of the Milky Way globular cluster NGC 7099, using deep *gr* photometry obtained with the Dark Energy Camera (DECam). We reached nearly 6 mag below the cluster Main Sequence (MS) turnoff, so that we dealt with the most suitable candidates to trace any stellar structure located beyond the cluster tidal radius. From star-by-star reddening corrected color-magnitude diagrams (CMDs) we defined four adjacent strips along the MS, for which we built the respective stellar density maps, once the contamination by field stars was properly removed. The resulting field star cleaned stellar density maps show a short tidal tail and some scattered debris. Such extra-tidal features are hardly detected when much shallower *Gaia* DR2 data sets are used and the same CMD field star cleaning procedure is applied. Indeed, by using 2.5 magnitudes below the cluster MS turnoff as the faintest limit ($G < 20.5$ mag), cluster members turned out to be distributed within the cluster's tidal radius, and some hints for field star density variations are found across a circle of radius 3.5° centered on the cluster and with similar CMD features as cluster stars. The proper motion distribution of these stars is distinguishable from that of the cluster, with some superposition, which resembles that of stars located beyond 3.5° from the cluster center.

Key words. Methods: observational - techniques: photometric - globular clusters: general - globular clusters: individual: NGC 7099.

1. Introduction

Tidal streams are witnesses of accreted dwarf galaxies disrupted by the Milky Way. They have been unveiled from wide-sky photometric and spectroscopic surveys, including Sloan Digital Sky Survey (SDSS)[1], Two Micron All-Sky Survey (2MASS)[2], Panoramic Survey Telescope and Rapid Response System (Pan-STARRS)[3], Dark Energy Survey (DES)[4] and *Gaia* mission[5]. The most spectacular example of these stellar substructures in the Milky Way halo is the one generated by the assimilation of the Sagittarius dwarf galaxy, which is moving around the Milky Way in an almost polar orbit (Ibata et al. 1994; Majewski et al. 2003; Belokurov et al. 2006; Koposov et al. 2012). Additional well-known streams in the Milky Way include the Monoceros ring, which may represent an on-plane accretion of a minor satellite, and the Sausage-Enceladus structure, which has been recently discovered in the *Gaia* DR2 (Belokurov et al. 2018; Helmi et al. 2018) and seems to be associated with the impact of an Small Magellanic Cloud-like mass galaxy on the Milky Way. There are also minor streams reported by Mateu et al. (2018) , as well as newly identified streams by Ibata et al. (2018).

Out of a family of ∼160 Galactic globular clusters, nearly 50 have been associated with one (or several) of the accreted galaxies and tidal streams discovered so far in the halo, based on their projected positions, kinematics and chemical abundances (Bellazzini et al. 2003; Forbes & Bridges 2010; Massari et al. 2019). However, the unambiguous confirmation of the extra-Galactic origin of one of the halo globular clusters requires the combination of multiple techniques and an important observational effort (see Carballo-Bello et al. 2017), so that most of the globular clusters on that list remain as candidates.

It has been thought that the structure of Milky Way globular clusters might provide precious information about their origin and accretion processes, as well as about the cluster internal dynamical evolution. Interestingly, many of the hypothetically accreted halo globular clusters show the signature of the presence of extra-tidal stars in the form of tidal tails (e.g., Pal 5, Odenkirchen et al. 2003) and extended halos (e.g., 47 Tuc, Piatti 2017a). For instance, in the case of the Sausage-Enceladus accretion event, most of the associated globular clusters proposed by Myeong et al. (2018) are embedded in a stellar component, which is only revealed using matched-filter techniques on deep wide-field photometry (Carballo-Bello et al. 2014; Vanderbeke et al. 2015; Kuzma et al. 2016; Carballo-Bello et al. 2018; Carballo-Bello 2019; Piatti & Carballo-Bello 2019). Whether

⋆ e-mail: andres.piatti@unc.edu.ar
[1] https://www.sdss.org
[2] https://irsa.ipac.caltech.edu/Missions/2mass.html
[3] https://panstarrs.stsci.edu
[4] https://www.darkenergysurvey.org
[5] https://gea.esac.esa.int/archive/

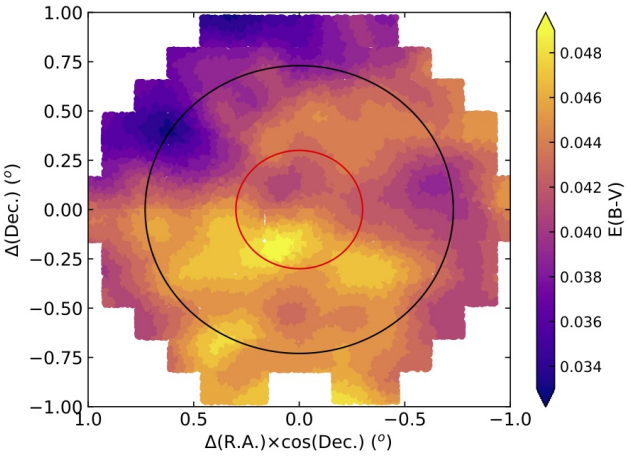

Fig. 1. Reddening map across the field of NGC 7099. The red and black circles are of 0.32° and 0.73° in radius, respectively. The black circle separates two areas of the same size.

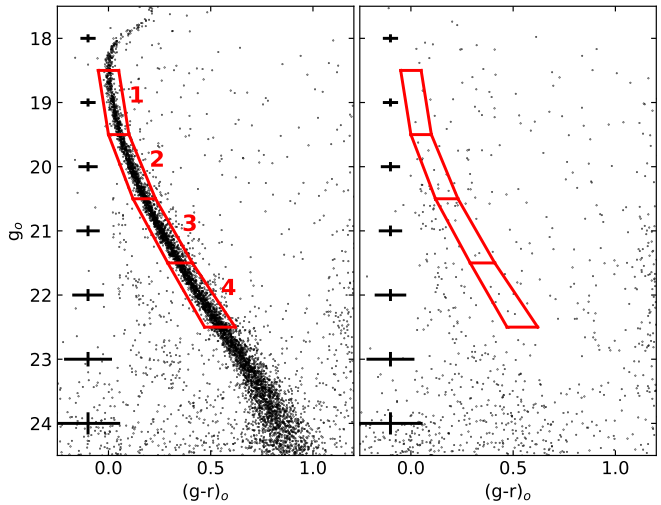

Fig. 2. CMDs of stars in the field of NGC 7099 ($r < 0.15°$; left panel) and in an annular region of same area centered on the cluster with an external radius of 0.8° (right panel). The four regions along the cluster MS used to perform star counts are delineated with red contour lines.

the outer structure of a globular cluster is defined by its formation conditions within a smaller protogalactic fragment or exclusively by its internal evolution and the orbit followed around the Milky Way, is one of the open questions in the study of Milky Way globular clusters (Massari et al. 2019; Piatti & Carballo-Bello 2020).

In this study we focus on NGC 7099, a poorly studied Milky Way globular cluster that might have been formed within the Sausage-Enceladus galaxy (Massari et al. 2019). With peri and apogalactocentric distances of 1.49 kpc and 8.15 kpc, respectively (Baumgardt et al. 2019), NGC 7099 moves along its retrograde orbit with a relatively high eccentricity and inclination angle (e= 0.69, i=61.5°, Piatti 2019), so that it could have crossed many times the inner disk regions. NGC 7099 has lost ∼ 30% of its initial mass by tidal heating caused by the Milky Way's gravitational field, in addition to another half of its initial mass by stellar evolution (Piatti et al. 2019). In Section 2, we describe the observational data collected, on which our analysis relies. Sections 2 and 3 detail the cleaning procedure applied to the observed NGC 7099 color-magnitude diagram (CMD) to get rid of the field star contamination, build the respective stellar density maps, and discuss our results in the light of recent findings (Sollima 2020, hereafter S20).

2. Data collection and processing

In this work we have used the Dark Energy Camera (DECam), which is mounted at the prime focus of the 4-m Blanco telescope at Cerro Tololo Inter-American Observatory (CTIO). DECam provides a 3 deg^2 field of view with its 62 identical chips with a scale of 0.263 arcsec pixel^{-1} (Flaugher et al. 2015). NGC 7099 was included among the targets of the observing program 2019B-1003 (08/09.08.2019) and the exposure times were 600×4 s and 600×4 s, for the g and r bands, respectively. We also observed 3–5 SDSS fields per night at different airmass to derive the atmospheric extinction coefficients and the transformations between the instrumental magnitudes and the SDSS *ugriz* system (Fukugita et al. 1996).

The images were processed by the DECam Community Pipeline (Valdes et al. 2014) and accessed via the NOAO Science Archive. The photometry was obtained from the images with the PSF-fitting algorithm of DAOPHOT II/ALLSTAR (Stetson 1987). The final catalog only includes stellar-shaped objects with $|sharpness| \leq 0.5$ to avoid as much as possible the presence of background galaxies and non-stellar sources in our analysis.

We also used DAOPHOT II to include in our images synthetic stars in order to estimate the completeness of our photometric catalogs. After applying our photometry pipeline, the limiting magnitude was set at the magnitude at which the synthetic stars are only recovered in 50% of the altered images. For g and r bands, the limiting magnitudes in our catalogs are 23.4 mag and 23.3 mag, respectively.

We retrieved the $E(B-V)$ values as a function of R.A. and Dec. from Schlafly & Finkbeiner (2011) provided by NASA/IPAC Infrared Science Archive[6] for the entire analyzed area. Figure 1 shows that the interstellar extinction along the line-of-sight is low, with a maximum difference between the most and least reddened regions of $\lesssim 0.02$ mag. Using Figure 1 we assigned individual $E(B-V)$ values to the measured stars according to their positions in the sky. In order to correct the observed magnitudes and colors by interstellar extinction, we used the individual $E(B-V)$ values and the A_λ/A_V coefficients given by Wang & Chen (2019). Aiming at illustrating the wealth of information we gathered, Figure 2 depicts the intrinsic CMD of the inner cluster region ($r < 0.15°$) and that of a sky annular region centered on the cluster with equivalent area and external radius of 0.8°. By comparing both panels of Figure 2 we conclude that the NGC 7099 CMD is affected by a low field contamination. Figure 2 also reveals a relatively narrow cluster MS, which extends more than 5 mag in g.

3. Stellar density maps

Because of two-body relaxation, less massive stars are candidates to escape the cluster more easily than more-massive ones (Balbinot & Gieles 2018). Hence, fainter cluster Main Sequence (MS) stars are usually employed to search for extra-tidal structures around globular clusters (see Piatti & Fernández-Trincado 2020, and references therein). We therefore take advantage the well-delineated MS shown in Figure 2 to define four adjacent

[6] https://irsa.ipac.caltech.edu/

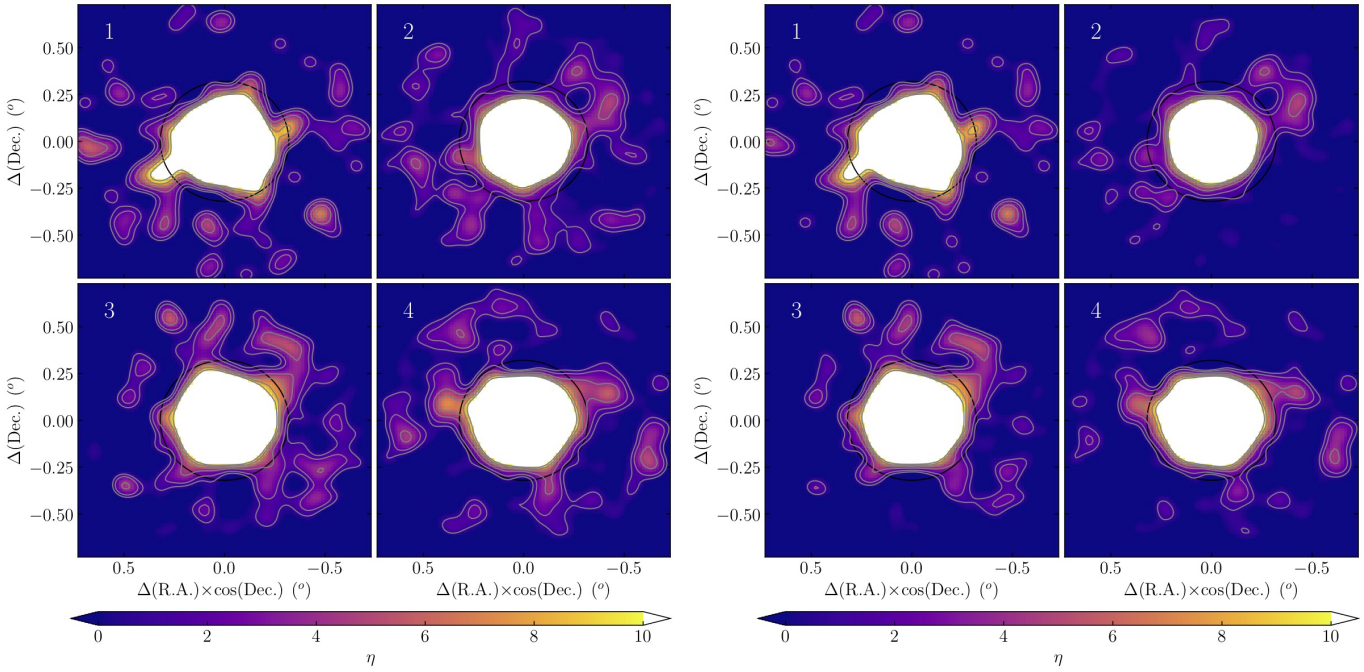

Fig. 3. Observed (left panels) and field star cleaned (right panels) stellar density maps for the four cluster MS strips of Figure 2 as labelled at the top-left margin of each panel. The black circle centered on the cluster indicates the assumed tidal radius. Contours for η = 1, 2, 4, 6, 8 and 10 are also shown; the colors follow the coding shown at the bottom of each panel.

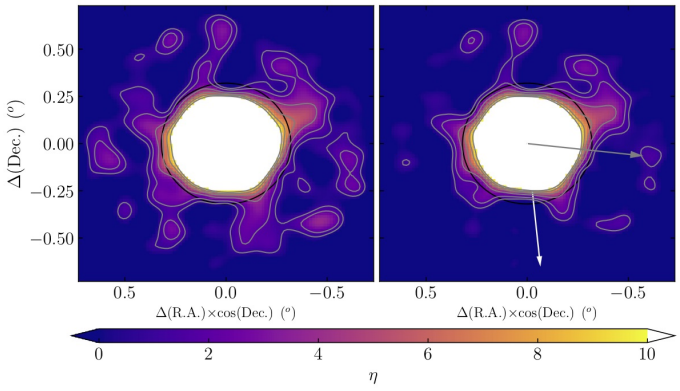

Fig. 4. Observed (left panel) and field star cleaned (right panel) stellar density maps

adding up all stars in the four cluster MS strips of Figure 2. The black circle centered on the cluster indicates the assumed tidal radius. Contours for η = 1, 2, 4, 6, 8 and 10 are also shown. The different arrows indicate the directions of the cluster proper motion (white) and of the Milky Way center (grey).

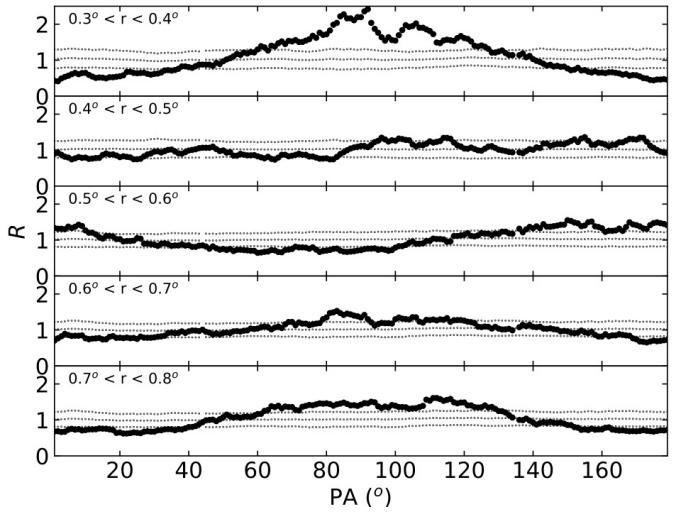

Fig. 5. The ratio R= $(N_c^A N_f^B)/(N_c^B N_f^A)$ (see Section 3 for details) versus PA obtained from star counts in the observed MS strip (large filled circles). Dotted lines represent the resulting mean and dispersion of the Monte Carlo simulations. The inset label indicates the annular region considered.

strips, from underneath the MS turnoff down to 4 mag below it, to map the distribution of their stellar populations. The cluster stellar density map is then straightforwardly constructed for the four different subsets of cluster MS stars.

Figure 3 shows the stellar density maps built for each MS strip using the AstroML (VanderPlas et al. 2012) kernel density estimator (KDE) routine. We superimposed a grid of 100×100 square cells on to the area of interest ($r < 0.73°$) and used a range of values for the KDE bandwidth from 0.02° up to 0.07° in steps of 0.01° in order to apply the KDE to each generated cell. We adopted a bandwidth of 0.05° as the optimal value. We also estimated the background level using the stars distributed within the annular region defined by the black circle in Figure 1 and an external radius of 0.8°. We divided such an annulus into 16 adjacent sectors of 22.5° wide, and counted the number of stars inside them. We rotated such an array of sectors by 11.25° and repeated the star counting. Finally, we derived the mean value in the 32 defined sectors, which turned out to be 35.5, 133.3, 114.0, and 100.0 stars/deg^2 for the MS strips #1 to 4, respectively. As for the standard deviation, we performed a thousand Monte Carlo realizations using the stars located beyond the red circle in Figure 1, which were rotated randomly (one different angle for each star) before recomputing the density map. The resulting standard deviation of all the generated density maps

turned out to be 20.3, 47.7, 41.4, and 44.6 stars/deg^2 for the MS strips #1 to 4, respectively. The color scale in Figure 3 represents the absolute deviation from the mean value in the field, in units of the standard deviation, that is, η = (signal − mean value)/standard deviation. We have painted white stellar densities with $\eta > 10$ in order to highlight the least dense structures. The same Monte Carlo procedure described above has been employed to determine the background density and its standard deviation in the cleaned CMD and have been used to calculate the value of η.

We applied a procedure to get rid of field stars that fall inside the four defined MS strips. The method was devised by Piatti & Bica (2012) and used satisfactorily for cleaning CMDs of star clusters projected towards crowded star fields (e.g., Piatti 2017b,c,a, and references therein) and affected by differential reddening (e.g., Piatti 2018; Piatti et al. 2018, and references therein). The method uses the magnitudes and colors of stars in a reference field CMD to subtract an equal number of stars in the cluster CMD that best resembles the reference field CMD. This is done by considering the position of each field star in the cluster CMD and by subtracting the closest star in the cluster CMD to that field star. The star-to-star subtraction in the cluster CMD is necessary to avoid stochastic effects and subtraction residuals, which arise when any fixed size for boxes homogeneously distributed throughout the CMD is chosen to count stars into them. We thus tightly reproduce the reference field CMD in terms of luminosity function, color distribution, and stellar density. The purpose of such a cleaning is to obtain a cluster CMD without field contamination. The contribution of field stars is included in the observed stellar density maps. The cleaning procedure subtracts exactly the number of field stars that contribute to the reference field CMD. The procedure searches throughout the whole cluster area for field stars to eliminate, giving the same chance (weight) to every subregion to contain such a field star. This is done to avoid spurious overdensities in the cleaned cluster field. If the star field were homogeneous and contained N stars per unit area, the procedure would subtract N stars per unit area. If there were any intrinsic spatial gradient of field stars in the cluster area, the procedure would eliminate it, at the expense of leaving some residuals as a counterpart of the excess of stars subtracted from the inner cluster region. If we did not considered the inner cluster region, the residuals would certainly decrease. In practice, for each reference field star, we randomly select an annular subregion in the cluster area where to subtract a field star. If no star in found in that annular sector, we randomly select another one and repeat the search, and allow to iterate the procedure up to 1000 times. The annular regions are 90° wide and of constant area. Their external radii are chosen randomly, while the internal ones are calculated so that the areas of the annular sectors are constant. Here we adopted an area equal to πr_{cls}, where r_{cls} is the cluster radius. If any stellar feature remains in the density map built from the cleaned cluster CMD, that is assumed to be an intrinsic cluster feature. The stellar density map built from stars in that CMD should have a background density close to zero. In doing this, we considered the uncertainties in magnitudes and colors by repeating the procedure hundreds of times with magnitudes and colors varying within their respective errors. For the designed MS strips, photometric errors increase from ≈ 0.04 mag up to 0.09 in g_0 and from ≈ 0.03 mag up to 0.11 mag in $(g - r)_0$ for the range $g_0 \approx$ 18- 23 mag. As for the reference star field, we chose the region embraced by the DECam boundaries and the black circle in Figure 1. We chose that region with the aim of dealing as close as possible with the intrinsic star field characteristics in the direction toward the cluster.

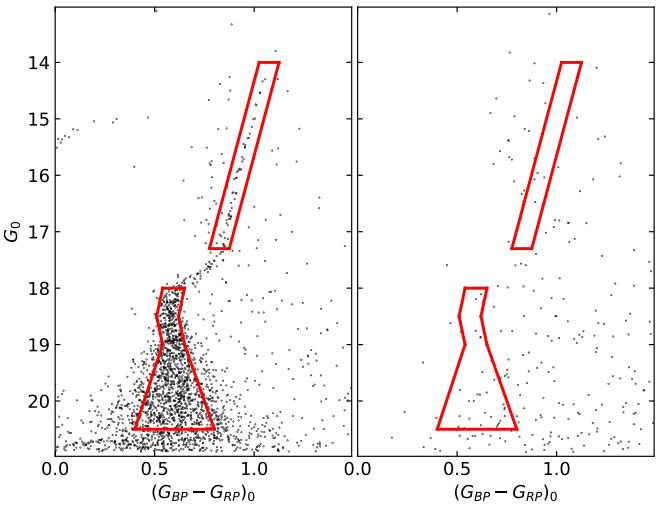

Fig. 6. *Gaia* color–magnitude diagrams of stars in the field of NGC 7099 ($r < 0.15°$; left panel) and in an annular region of same area centered on the cluster with an external radius of 0.8° (right panel). The RGB and MS regions used to perform star counts are delineated with red contour lines.

Its stellar density does not show any dependence as a function of the position angle for any of the four MS strips.

The field star cleaned stellar density maps were built similarly as the observed ones, and are shown in Figure 3. They reveal a short tail, which resembles that of S20 for the same area, and some stellar debris distributed beyond the tidal radius of NGC 7099 (0.32° Harris 1996; Piatti et al. 2019). Although the MS strips #1 to 4 include stars with different masses, in the sense that the fainter the MS strip the less massive its stars, we do not find any remarkable difference between density maps. We would have expected more extended extra-tidal features to show up in the case of the lowest-mass bins, as lower-mass stars can be more easily stripped away from the cluster than their higher-mass counterparts. For this reason, we also produced a stellar density map with all the stars in the MS strips #1 to 4. Figure 4 depicts the resulting stellar density maps, where evidence of a short tidal tail would seem to arise clearer.

We further analyzed the possibility of tidal deformations across the cluster stellar density map, in the sense that preferential orientation toward the Galactic center and along the direction of the orbit of the cluster are expected in the innermost and outermost parts, respectively (Montuori et al. 2007). We followed the recipe applied by Sollima et al. (2011) based on counts of cluster MS strip stars in alternate pairs of circular sectors of 90° in width located at a given distance from the cluster center and oriented at a position angle (PA) in opposite directions. PA is measured from the North anti-clockwise. We then computed the ratio $R(PA) = (N_c^A N_f^B)/(N_c^B N_f^A)$, where A and B are the pair of alternate sectors, and c and f refer to the cluster MS strip and a CMD field rectangle defined by $18.5 < g_0$ (mag) < 22.5 and $1.0 < (g-r)_0$ (mag) < 1.15. In order to assess the statistical significance of our results, we performed 1000 Monte Carlo realizations using the same number of measured stars distributed randomly in PA and then obtained the mean and standard deviations of those independent executions. Figure 5 depicts the resulting curves for different annular regions. As suggested by Figure 4, Figure 5 shows the existence of a short tidal tail nearly aligned with direction to the Milky Way center, in very good agreement with Montuori et al. (2007)'s models. The PA's width of this short tail

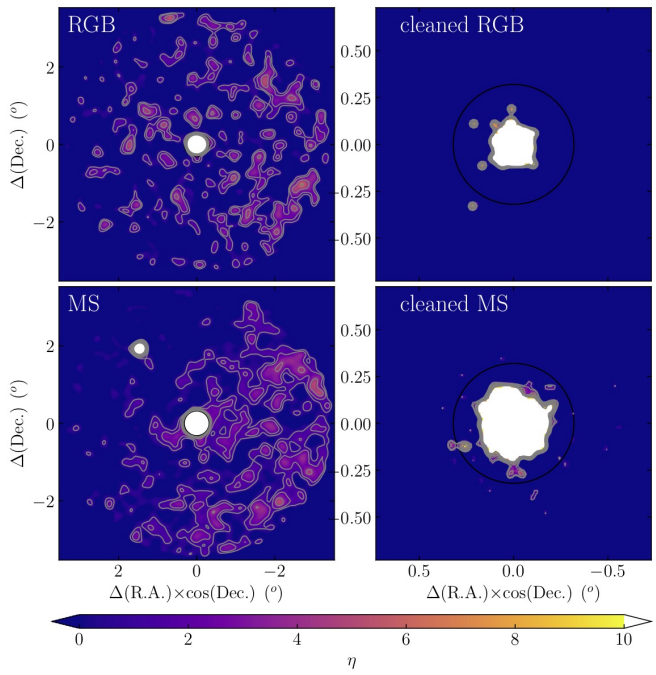

Fig. 7. *Gaia* observed (left panels) and field star cleaned (right panels) stellar density maps for the cluster RGB and MS strips of Figure 6. The black circle centered on the cluster indicates the assumed tidal radius.

also agrees with S20 (see his Figure 4). For completeness purposes we included in Fig. 4 (right panel) the directions toward the Milky Way center and of the motion of the cluster.

We estimated the g surface brightness of the tidal tail observed in Fig. 4, i.e., from the stars that were not subtracted by the field star cleaned CMD procedure, for three different adjacent annulus of 0.1° wide, located between 0.4° and 0.7° from the cluster center. We first calculated the integrated g magnitude (g_{int}) for stars located inside a radius of 0.1° from the cluster center in Fig. 4 (right panel), by summing de DECam g fluxes of individual stars. A normalization constant c was calculated as :

$c = g_{int0} + 2.5 \times log(N_0/\pi 0.1^2)$

where N_0 represents the number of stars used. Then, the integrated magnitudes for the different annular regions were calculated according to:

$g_{int} = c - 2.5 \times log(N/(\pi(r_2^2 - r_1^2)))$

where N, r_1, and r_2 represent the number of stars located in an annulus with inner and outer radii r_1 and r_2, respectively. With the aim of expressing the integrated magnitudes in units of V mag per square arcsec, we used the integrated $B - V$ color for NGC 7099 listed by Harris (=0.60 mag; 1996, 2010 Edition) and the linear relationship between g and V in terms of the $B - V$ color (Jordi et al. 2006). The resulting surface brightness and its uncertainty computed from propagation of errors assuming a Poisson statistics turned out to be 31.35±0.11, 31.41±0.11, and 31.44±0.12 mag per square arcsec for the annulus at r = 0.4°-0.5°, 0.5°-0.6°, and 0.6°-0.7°, respectively.

4. Discussion

Recently, S20 presented results of a 5D mixture modelling technique based on *Gaia* DR2 data of the outer regions of 18 Milky Way globular clusters. He found that NGC 7099 has long tidal tails. Reportedly, those tails are composed by cluster red giant branch (RGB) and MS stars reaching down to ∼ 1 mag below the MS turnoff of the cluster. This means that S20 used stars on average brighter than those of our selected MS strip #1 in Figure 2. At this point, we wonder what caused the different results obtained in the present study compared to those in S20, particularly because MS stars in strips #2 to 4 are expected to be better candidates to trace extra-tidal structures. According to S20 (his Figure 1), selected MS stars have parallaxes within a range at least 10 times larger than the parallaxes of RGB stars, which means that field stars with loci in the CMD and in the vector point diagram (VPD, proper motion in R.A. (pmra) vs. proper motion in Dec. (pmdec)) similar to those of the cluster stars could be included in the selected sample. From a comparison of previous studies on the outer regions of Milky Way globular clusters (see Table 1 in Piatti & Carballo-Bello 2020), we also found that results for some globular clusters are distinct from those found in S20. For instance, NGC 1851 and 4590 are known to have long tidal tails, although not detected in S20, while NGC 2298, 6341, and 6362 seem not to have the tails traced in S20. To this respect, we note that it is not straightforward to conclude whether deep photometric-only data sets or shallow proper motion-selected ones are preferable to detect tidal tails. Therefore, it is conceivable that differences can be found in some globular clusters subject to different levels of contaminations when analyzing them with different data sets.

We used the 5° in radius around NGC 7099 *Gaia* DR2 (Gaia Collaboration et al. 2016, 2018) database as in S20 to repeat the CMD cleaning procedure applied in Section 3, in order to build a stellar density map to be compared with that produced by S20. Figure 6 shows the intrinsic CMD of the inner cluster region used in Figure 2 that highlights the main features of NGC 7099. Particularly, we chose a strip along the RGB and another one from the MS turnoff down to 2.5 mags underneath. According to Arenou et al. (2018, see Section 3), the *Gaia* DR2 photometry completeness is 90% for stars with $G < 19$ mag in the inner region of a globular cluster with $\sim 10^4$ stars/sq deg, so that we deal with basically a complete photometry data set. The adopted fainter limit should be likewise aceptable to guarantee the homogeneity of the completeness. We also used a bandwidth of 0.1° in order to get the highest contrast of tidal tails. We cleaned both strips from field star contamination for a circular area centered on NGC 7099 with radius equal to 3.53°, in order to ensure a reference field star region ($3.53° < r < 5°$) with an equal cluster area. The *Gaia* photometry was corrected by reddening using individual $E(B - V)$ values obtained from Schlafly & Finkbeiner (2011), and the relationships $A_G = 2.44E(B - V)$ and $E(G_{BP} - G_{RP}) = 1.27E(B - V)$ (Wang & Chen 2019). The observed and cleaned stellar density maps are depicted in Figure 7. Observed RGB and MS density maps exhibit different spatial distributions, the latter suggesting the existence of tidal tails within a remarkably non-uniform star field spatial distribution. Long tidal tails do not remain in the star field cleaned density maps, although some hint for short ones are found.

The above outcomes suggest that stars distributed along the cluster CMD features (e.g., strips in Figures 2 and 6) located beyond its tidal radius ($r > 0.32°$) might belong to the Milky Way field. We further used the proper motions of all the stars located within the strips drawn in Fig. 6, which show some particular features. We illustrate them in Figure 8, where we plotted the VPD for RGB and MS strip stars located in three different sky regions, namely, those located inside the tidal radius of the cluster (top panels), those distributed between 0.32° and 3.53° from the cluster center (middle panels), and those adopted as reference field stars (bottom panels). Cluster stars (g_0(MS strip) < 19 mag) and RGB strip stars) have a well-defined distribution

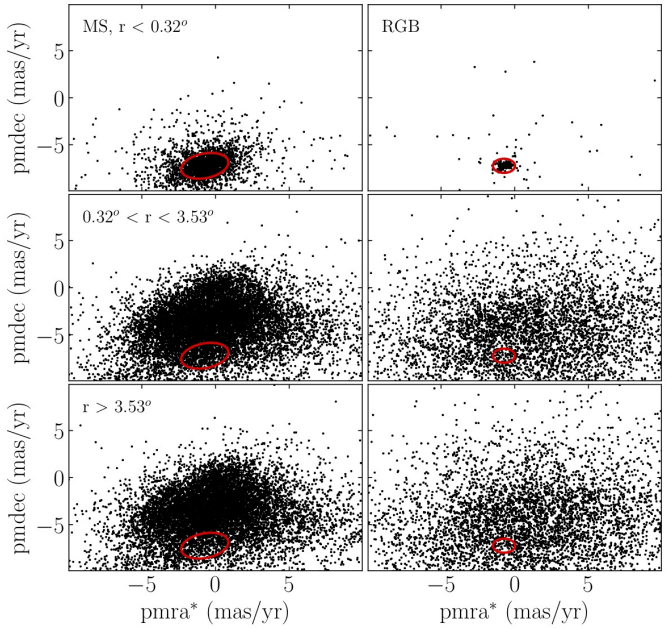

Fig. 8. Vector point diagrams for RGB (right panels) and MS (left panels) strips of Figure 6 for different annular regions. Red ellipses that mostly embrace cluster stars in the top panels were superimposed onto the middle and bottom panels.

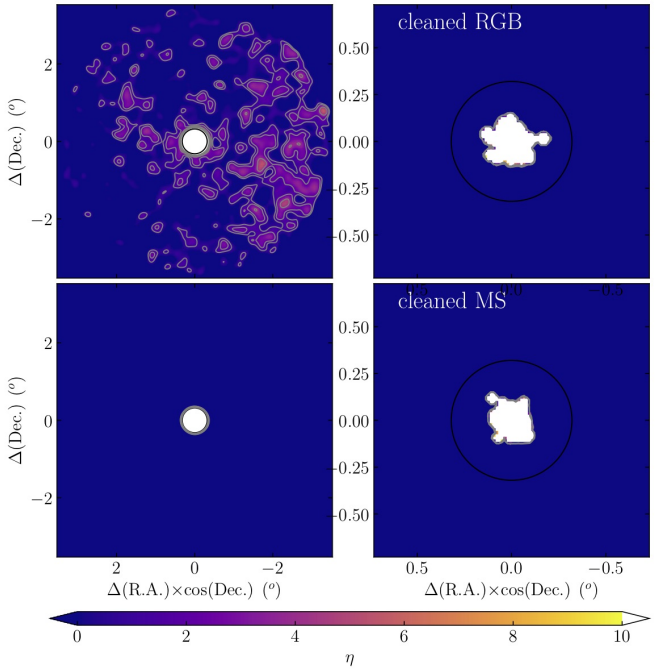

Fig. 9. *Gaia* observed (top-left panel) and field star cleaned (bottom-left panel) stellar density maps for stars selected only from proper motion and parallax criteria. The right panels correspond to RGB and MS stars that remained unsubtracted after the photometric and kinematic cleaning procedures were applied.The black circle centered on the cluster indicates the assumed tidal radius.

in the VPD, which we embraced by a red ellipse (top panels). Stars located beyond the cluster radius have a different distribution (middle and bottom panels), with some superposition with that of cluster stars (top panels). For comparison purposes, we superimposed the ellipses in the top panels onto the middle and bottom panels. The middle panel reveals that there are many MS strip stars located outside the cluster with proper motions distinguishable from that of the cluster (most of the stars located outside the ellipses). Particularly, they have g_0 mag between 19 and 20.5 mag (see Figure 6). Most of those stars were eliminated using the CMD cleaning procedure (see Fig. 7).

From Figure 8 we conclude that out of all the stars distributed within the RGB and MS strips, some of them have sky projected kinematics similar to that of cluster stars. Therefore, an unavoidable question arises: are those stars cluster members? If we used the CMD cleaning procedure, we would answer that they do not belong to the cluster population, as obtained above. Indeed, we clean from field star contamination the VPD at $r < 3.53°$ from the cluster center, using as a reference a star field located between 3.53° and 5°, similarly as we carried out for the CMD cleaning. The resulting star field cleaned stellar density maps for RGB and MS strip stars that share the cluster's proper motion, built using the same bandwidth as in Figure 7, do not show any extra-tidal feature (see Fig. 9, right panels). Finally, we used only the kinematic and parallax information for selecting cluster stars. The top-left panel of Fig. 9 shows the stellar density map built for stars with proper motions within an ellipse centered on (-0.73 mas/yr,-7.24 mas/yr), width=3.4 mas/yr, height=2.5 mas/yr and angle=30°, and $|\varpi| < 5\sigma(\varpi)$ (S20), while the bottom-left one depicts the stellar density map after cleaning the cluster field from field contamination, based only on the kinematic information. As can be seen, there is not any remaining signature of extra-tidal features.

5. Conclusions

In this study we analyze the outer regions of the Milky Way globular cluster NGC 7099, aiming at identifying extra-tidal features. The cluster caught our attention because it was claimed that it might have formed within the accreted Sausage-Enceladus dwarf galaxy and deposited in an inner halo orbit, with relatively high eccentricity and inclination angle with respect to the Milky Way plane. According to Piatti et al. (2019), globular clusters with orbital parameters like those of NGC 7099 have lost relatively more mass by tidal disruption than globular clusters rotating in the Milky Way disk. In the case of NGC 7099, the disrupted mass to the initial mass ratio is 0.30.

We carried out DECam observations that, as far as we are aware, allowed us to build the deepest cluster CMD, reaching ~ 6 mags beneath its MS turnoff. Those observed faint MS stars are treated as suitable candidates to trace extra-tidal features, because they are the first to cross the Jacobi radius once they reach the cluster boundary driven by two-body relaxation. Indeed, it has long been observed that the brighter the range of magnitudes considered, the sharper the cluster stellar radial profile.

In order to monitor any differential change in the stellar density map caused by cluster stars with distinct brightnesses, we split the long cluster MS into four segments of one mag long each, and analyzed them separately. We built their respective stellar density maps with a frequently used KDE technique, once the magnitudes and colors of the stars were individually corrected by the interstellar extinction. When a statistical decontamination method is used to clean the cluster CMD from field stars, the resulting cleaned stellar density maps show a short tidal tail and some scattered debris. The short tidal tail is nearly oriented to the Milky Way center, as expected for innermost parts of tidal tails. We did not found these extra-tidal features when analyz-

ing *Gaia* data with the same cleaning procedure. In this case, the photometry used is much shallower than the DECam photometry, reaching 2.5 magnitudes below the cluster MS turnoff, and the analyzed area 25 times larger than afforded by our DECam data, so that the reference star field is located much farther from the cluster ($3.53^\circ < r < 5.00^\circ$).

RGB and MS strip stars located inside and outside the cluster tidal radius (0.32°) present distinguishable VPDs, with some superposition. When comparing their VPDs, using the CMD cleaning method separately, for stars located within a circle of radius 3.53° with those placed in the reference star field ($3.53^\circ < r < 5.00^\circ$), we did not find any extra-tidal feature. S20 detected long tidal tails, the innermost parts of them also found from DECam data. Finally, we would like to mention that extra-tidal stars should have distinct velocities that make them possible to escape the cluster. Likewise, they are at different Galactocentric distances than the cluster itself, so that they are differently affected by the Milky Way gravitational field (Piatti 2020; Dinnbier & Kroupa 2020).

Acknowledgements. We thank the referee for the thorough reading of the manuscript and timely suggestions to improve it. Support for M.C. is provided by ANID Millennium Science Initiative grant ICN12_009; by Proyecto Basal AFB-170002; and by FONDECYT grant 1171273. Based on observations at Cerro Tololo Inter-American Observatory, NSF's NOIRLab (Prop. ID 2019B-1003; PI: Carballo-Bello), which is managed by the Association of Universities for Research in Astronomy (AURA) under a cooperative agreement with the National Science Foundation. This project used data obtained with the Dark Energy Camera (DECam), which was constructed by the Dark Energy Survey (DES) collaboration. Funding for the DES Projects has been provided by the US Department of Energy, the US National Science Foundation, the Ministry of Science and Education of Spain, the Science and Technology Facilities Council of the United Kingdom, the Higher Education Funding Council for England, the National Center for Supercomputing Applications at the University of Illinois at Urbana-Champaign, the Kavli Institute for Cosmological Physics at the University of Chicago, Center for Cosmology and Astro-Particle Physics at the Ohio State University, the Mitchell Institute for Fundamental Physics and Astronomy at Texas A&M University, Financiadora de Estudos e Projetos, Fundação Carlos Chagas Filho de Amparo à Pesquisa do Estado do Rio de Janeiro, Conselho Nacional de Desenvolvimento Científico e Tecnológico and the Ministério da Ciência, Tecnologia e Inovação, the Deutsche Forschungsgemeinschaft and the Collaborating Institutions in the Dark Energy Survey. The Collaborating Institutions are Argonne National Laboratory, the University of California at Santa Cruz, the University of Cambridge, Centro de Investigaciones Enérgeticas, Medioambientales y Tecnológicas–Madrid, the University of Chicago, University College London, the DES-Brazil Consortium, the University of Edinburgh, the Eidgenössische Technische Hochschule (ETH) Zürich, Fermi National Accelerator Laboratory, the University of Illinois at Urbana-Champaign, the Institut de Ciències de l'Espai (IEEC/CSIC), the Institut de Física d'Altes Energies, Lawrence Berkeley National Laboratory, the Ludwig-Maximilians Universität München and the associated Excellence Cluster Universe, the University of Michigan, NSF's NOIRLab, the University of Nottingham, the Ohio State University, the OzDES Membership Consortium, the University of Pennsylvania, the University of Portsmouth, SLAC National Accelerator Laboratory, Stanford University, the University of Sussex, and Texas A&M University.

References

Arenou, F., Luri, X., Babusiaux, C., et al. 2018, A&A, 616, A17
Balbinot, E. & Gieles, M. 2018, MNRAS, 474, 2479
Baumgardt, H., Hilker, M., Sollima, A., & Bellini, A. 2019, MNRAS, 482, 5138
Bellazzini, M., Ferraro, F. R., & Ibata, R. 2003, AJ, 125, 188
Belokurov, V., Erkal, D., Evans, N. W., Koposov, S. E., & Deason, A. J. 2018, MNRAS, 478, 611
Belokurov, V., Zucker, D. B., Evans, N. W., et al. 2006, ApJ, 642, L137
Carballo-Bello, J. A. 2019, MNRAS, 486, 1667
Carballo-Bello, J. A., Corral-Santana, J. M., Martínez-Delgado, D., et al. 2017, MNRAS, 467, L91
Carballo-Bello, J. A., Martínez-Delgado, D., Navarrete, C., et al. 2018, MNRAS, 474, 683
Carballo-Bello, J. A., Sollima, A., Martínez-Delgado, D., et al. 2014, MNRAS, 445, 2971
Dinnbier, F. & Kroupa, P. 2020, arXiv e-prints, arXiv:2006.14087
Flaugher, B., Diehl, H. T., Honscheid, K., et al. 2015, AJ, 150, 150
Forbes, D. A. & Bridges, T. 2010, MNRAS, 404, 1203
Fukugita, M., Ichikawa, T., Gunn, J. E., et al. 1996, AJ, 111, 1748
Gaia Collaboration, Brown, A. G. A., Vallenari, A., et al. 2018, A&A, 616, A1
Gaia Collaboration, Prusti, T., de Bruijne, J. H. J., et al. 2016, A&A, 595, A1
Harris, W. E. 1996, AJ, 112, 1487
Helmi, A., Babusiaux, C., Koppelman, H. H., et al. 2018, Nature, 563, 85
Ibata, R. A., Gilmore, G., & Irwin, M. J. 1994, Nature, 370, 194
Ibata, R. A., Malhan, K., Martin, N. F., & Starkenburg, E. 2018, ApJ, 865, 85
Jordi, K., Grebel, E. K., & Ammon, K. 2006, A&A, 460, 339
Koposov, S. E., Belokurov, V., Evans, N. W., et al. 2012, ApJ, 750, 80
Kuzma, P. B., Da Costa, G. S., Mackey, A. D., & Roderick, T. A. 2016, MNRAS, 461, 3639
Majewski, S. R., Skrutskie, M. F., Weinberg, M. D., & Ostheimer, J. C. 2003, ApJ, 599, 1082
Massari, D., Koppelman, H. H., & Helmi, A. 2019, A&A, 630, L4
Mateu, C., Read, J. I., & Kawata, D. 2018, MNRAS, 474, 4112
Montuori, M., Capuzzo-Dolcetta, R., Di Matteo, P., Lepinette, A., & Miocchi, P. 2007, ApJ, 659, 1212
Myeong, G. C., Evans, N. W., Belokurov, V., Sanders, J. L., & Koposov, S. E. 2018, ApJ, 863, L28
Odenkirchen, M., Grebel, E. K., Dehnen, W., et al. 2003, AJ, 126, 2385
Piatti, A. E. 2017a, ApJ, 846, L10
Piatti, A. E. 2017b, ApJ, 834, L14
Piatti, A. E. 2017c, MNRAS, 465, 2748
Piatti, A. E. 2018, MNRAS, 477, 2164
Piatti, A. E. 2019, ApJ, 882, 98
Piatti, A. E. 2020, arXiv e-prints, arXiv:2006.04688
Piatti, A. E. & Bica, E. 2012, MNRAS, 425, 3085
Piatti, A. E. & Carballo-Bello, J. A. 2019, MNRAS, 485, 1029
Piatti, A. E. & Carballo-Bello, J. A. 2020, A&A, 637, L2
Piatti, A. E., Cole, A. A., & Emptage, B. 2018, MNRAS, 473, 105
Piatti, A. E. & Fernández-Trincado, J. G. 2020, A&A, 635, A93
Piatti, A. E., Webb, J. J., & Carlberg, R. G. 2019, MNRAS, 489, 4367
Schlafly, E. F. & Finkbeiner, D. P. 2011, ApJ, 737, 103
Sollima, A. 2020, MNRAS, 495, 2222
Sollima, A., Martínez-Delgado, D., Valls-Gabaud, D., & Peñarrubia, J. 2011, ApJ, 726, 47
Stetson, P. B. 1987, PASP, 99, 191
Valdes, F., Gruendl, R., & DES Project. 2014, in Astronomical Society of the Pacific Conference Series, Vol. 485, Astronomical Data Analysis Software and Systems XXIII, ed. N. Manset & P. Forshay, 379
Vanderbeke, J., De Propris, R., De Rijcke, S., et al. 2015, MNRAS, 450, 2692
VanderPlas, J., Connolly, A. J., Ivezic, Z., & Gray, A. 2012, in Proceedings of Conference on Intelligent Data Understanding (CIDU), 47–54
Wang, S. & Chen, X. 2019, ApJ, 877, 116